

## Numerical simulations of dense granular suspensions in laminar flow under constant and varying shear rates

Srinivasan, Sudharsan; Van den Akker, Harry E.A.; Shardt, Orest

**DOI**

[10.1016/j.compfluid.2021.105115](https://doi.org/10.1016/j.compfluid.2021.105115)

**Publication date**

2021

**Document Version**

Final published version

**Published in**

Computers and Fluids

**Citation (APA)**

Srinivasan, S., Van den Akker, H. E. A., & Shardt, O. (2021). Numerical simulations of dense granular suspensions in laminar flow under constant and varying shear rates. *Computers and Fluids*, 230, Article 105115. <https://doi.org/10.1016/j.compfluid.2021.105115>

**Important note**

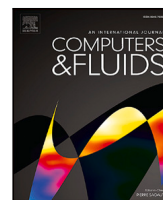
To cite this publication, please use the final published version (if applicable). Please check the document version above.

**Copyright**

Other than for strictly personal use, it is not permitted to download, forward or distribute the text or part of it, without the consent of the author(s) and/or copyright holder(s), unless the work is under an open content license such as Creative Commons.

**Takedown policy**

Please contact us and provide details if you believe this document breaches copyrights. We will remove access to the work immediately and investigate your claim.



# Numerical simulations of dense granular suspensions in laminar flow under constant and varying shear rates

Sudharsan Srinivasan<sup>a,b,\*</sup>, Harry E.A. Van den Akker<sup>a,b,c</sup>, Orest Shardt<sup>a,b,\*\*</sup>

<sup>a</sup> Synthesis and Solid State Pharmaceutical Centre (SSPC), University of Limerick, V94T9PX, Limerick, Ireland

<sup>b</sup> Bernal Institute and School of Engineering, University of Limerick, V94T9PX, Limerick, Ireland

<sup>c</sup> Transport Phenomena Lab, Department of Chemical Engineering, Delft University of Technology, Van der Maasweg 9, 2629 HZ Delft, The Netherlands

## ARTICLE INFO

### Keywords:

Suspensions  
Rheology  
Shear reversal  
Time-varying shear  
Immersed boundary-lattice Boltzmann method

## ABSTRACT

Using an immersed boundary-lattice Boltzmann method, we investigated the response of dense granular suspensions to time-varying shear rates and flow reversals. The evolution of the relative apparent viscosity and particle structures was analysed. The concentration of solids ( $\phi_v$ ) and particle Reynolds numbers ( $Re_p$ ) were varied over the ranges  $6\% \leq \phi_v \leq 47\%$  and  $0.105 \leq Re_p \leq 0.529$ . The simulations included sub-grid scale corrections for unresolved lubrication forces and torques (normal and tangential). When  $\phi_v$  surpasses 30%, the contribution of the tangential lubrication corrections to the shear stress is dominant. While for intermediate solids fractions we find weak shear-thinning, we see weak shear-thickening for  $\phi_v > 40\%$ . We show how the structure and apparent viscosity of a suspension evolves after a reversal of the shear direction. For 47% solids, simulations with step changes in the shear rate show the effects of the previous shear history on the viscosity of the suspension.

## 1. Introduction

Suspensions are complex fluids and their rheology is determined by the characteristics of the suspended particles and their interactions. Although hydraulic transport of dense solids suspensions is typical practice in many processes, such as wastewater treatment, drilling operations, and ore refining plants, operating such transport lines frequently results in significant disruptions. Improved understanding of the complicated dynamics of particle-particle and fluid-particle interactions is thus highly desirable. Specifically, changes in the rheology and structure that occur due to the effects of flow reversals and abrupt shifts in the shear rate are of particular interest to us, as the transport of slurry involves such phenomena in bends, fittings, and valves. In our previous study [1], we explored the effects of steady shear rate on rheology by implementing a spring-like force to handle particle collisions. In this paper, we improve the modelling of interparticle interactions by applying explicit lubrication corrections over sub-grid scale distances, so that the resulting simulation can provide a better understanding of both the steady-state and transient rheological behaviour of granular suspensions. We restrict ourselves to suspensions of particles typically some 300  $\mu\text{m}$  in diameter, with solids volume fractions  $\phi_v$  between 6 and 47%, and particle Reynolds numbers  $Re_p$  between 0.105 and 0.529.

Over the last few decades, research on the rheology of suspensions has advanced through both experimental and computational studies. Brady and Bossis [2] used Stokesian dynamics to investigate the apparent viscosity (the ratio of the effective viscosity over the viscosity of the suspending fluid) of concentrated suspensions. Jogun and Zukoski [3] conducted experiments with plate-like particles suspended inside a basic solution to study its rheological behaviour (the yielding type of response). A review article by Stickel and Powell [4] also discusses the rheology of dense suspensions with more emphasis on microstructure and total fluid stresses. The non-Newtonian behaviour of dense suspensions, such as normal-stress differences and shear-induced migration, has been discussed by Guazzelli [5] and co-workers [6]. By coupling the Lattice Boltzmann Method (LBM) with a hybrid Immersed Boundary Method (IBM) and a bounce-back scheme, Lorenz et al. [7] demonstrated the continuous and discontinuous shear thickening of concentrated suspensions. Both [8] and [1] performed numerical simulations using LBM — the former discussed the effects of particle concentration and density ratio on the viscosity of suspensions, while the latter discussed the role of particle rotation and cluster formation on the shear thickening of suspensions.

Suspension properties are well known in dilute regimes [9,10]. However, as the concentration of solids increases, the rheological

\* Corresponding author at: Synthesis and Solid State Pharmaceutical Centre (SSPC), University of Limerick, V94T9PX, Limerick, Ireland.

\*\* Corresponding author at: Bernal Institute and School of Engineering, University of Limerick, V94T9PX, Limerick, Ireland.

E-mail addresses: [Sudharsan.Srinivasan@ul.ie](mailto:Sudharsan.Srinivasan@ul.ie) (S. Srinivasan), [Harry.VanDenAkker@ul.ie](mailto:Harry.VanDenAkker@ul.ie) (H.E.A. Van den Akker), [Orest.Shardt@ul.ie](mailto:Orest.Shardt@ul.ie) (O. Shardt).

properties of suspensions become more complicated. While many researchers have reported the steady-state rheology of suspensions [11–13], few have studied their transient behaviour. The time-dependent response of the relative apparent viscosity of a dense suspension may arise due to a change in the magnitude of the shear rate or a reversal of the direction of the shear flow. Gadala-Maria and Acrivos [14] reported the first experimental observation of the response of shear stress to a reversal of the flow direction. Experiments with spherical particles in the Couette device showed that for solid fractions  $\phi_v > 30\%$ , the memory effects of previous shearing were evident when the shear was stopped and then resumed in either the same or opposite direction. Both [15] and [16] conducted experiments to demonstrate the transient evolution of suspensions after reversing the direction of flow.

In recent years, interpretation of the transient rheology of suspensions through numerical simulation is gaining more attention. For instance, Srinivasan et al. [1] examined the history-dependent rheology of suspensions at finite inertia when subjected to a sudden increase and decrease in the shear rate. Simulations of suspensions in Stokes flow submitted to shear reversal have been reported by Peters et al. [17]. However, the aspects of some of the underlying characteristics of the suspension dynamics, such as the time scales that govern the development of wall shear stress (for particles with finite inertia, i.e.  $Re_p$  of order  $10^{-1}$ ) after flow reversal, are often not considered.

We have developed an in-house numerical code to simulate solid-liquid suspensions using IB-LBM [1]. We now improve the simulations by modifying the sub-grid scale force from the previously applied spring model to lubrication corrections [18–20]. While the IB-LBM simulations resolve the flow and provide an accurate value of the force on particle over larger interparticle gaps, corrections for unresolved normal and tangential lubrication corrections (which we denote as NTLC in the remainder of the paper) are turned on when the gap size between the adjacent particles is smaller than a selected cutoff (on the order of the computational grid size). We choose the cutoff such that it restores the correct behaviour of the force on the particles in the limit of small interparticle gaps, with the understanding that the forces calculated for intermediate gap sizes are not strictly accurate — although they do interpolate well between the two extremes.

In this work, we analyse both the steady-state and time-dependent rheology of dense suspensions (up to 47% solids by volume) under simple shear flow. In particular, we focus on the effects of particle volume fraction and shear rate (expressed in terms of  $Re_p$ ) by considering the simulations of suspensions that are subjected to:

- an instantaneous reversal of the direction of shear flow,
- increases and decreases in the shear speed in one step, and
- a sudden stop and then a restart of the fluid flow.

The main purpose of this paper is to improve the results of our previous study [1] by including the contribution of lubrication corrections and to understand the suspension behaviour in time-varying shear flows. Quantitatively, the significance of the two time scales (viscous and advective) that control the transients after shear reversal is shown. For the range of  $\phi_v$  and  $Re_p$  considered, we also show that our findings are consistent with the results reported by Krieger and Dougherty [21], Dbouk et al. [12], Thorimbert et al. [8], and Srinivasan et al. [1].

This paper is arranged in the following way: In Section 2, we summarise our problem statement. In Section 3, we briefly describe the immersed boundary-lattice Boltzmann method. In the remainder of Section 3, we first discuss the implementation of the sub-grid scale normal lubrication correction (referred to as NLC), the specifics of the integration of particle motion, and finally show how the relative apparent viscosity is computed from the stress on the moving walls. In Section 4.1, we present the results of steady-state rheology of suspensions. Then, in Section 4.2, we discuss the simulations of the effects of shear reversal followed by the simulations of suspensions subjected to step changes in the magnitude of shear rate in Section 4.3. In the final Section 5, we provide our conclusions. Appendix A deals with

the lubrication force and torque expressions for particles interacting with walls, while Appendix B specifies the initial particle positions for varying solids volume fractions.

## 2. Problem statement

The transport of slurry through industrial pipelines has inspired us to carry out the current numerical analysis. The dynamics of such transport are complex due to the transient fluctuations in the flow rate and spatial variations along the line (e.g., bends and valves). In this application, the concentration of solids amounts to some 35%, and particles have finite inertia with particle Reynolds number typically of  $O(10^{-1})$ , and the flow is laminar. The carrier liquid phase is Newtonian with kinematic viscosity  $\nu$ . We model the suspensions as consisting of monodisperse rigid spheres that are 300  $\mu\text{m}$  in diameter, which is typical for the slurries we are interested in.

While our current numerical analysis is intended to mimic a representative volume of suspension within a macroscopic flow, simulation domain dimensions and boundary conditions are similar to the parameters of a rheometer. A typical case is a suspension of 300  $\mu\text{m}$  diameter particles in a standard rheometer with a 2 mm gap, resulting in a confinement ratio  $\delta = 2R/H = 0.15$  (where  $R$  denotes particle radius and  $H$  is the gap width). In our suspension simulations, the confinement ratio is 0.16, with  $R = 4$  lu and  $H = 50$  lu, where lu denotes lattice units (multiples of the simulation grid size).

A schematic of the simulation domain with particles suspended between two parallel plates is presented in Fig. 1. These plates move in opposite directions with a speed  $U_w$ , and we define  $U^* = U_x/U_w$  (where  $U_x$  is the  $x$  component of the liquid velocity). The particles are placed randomly between the parallel walls. The flow is induced only by the shearing motion of the walls, and we do not take into account the effects of gravity. The imposed shear rate is  $\dot{\gamma} = 2U_w/H$ . The simulation box is periodic in the flow ( $x$ ) and vorticity ( $y$ ) directions. We determine the relative apparent viscosity of the suspension under steady-state and transient conditions by varying the wall speed (shear rate) and the number of particles (solids volume fraction).

## 3. Simulation methods

### 3.1. The immersed boundary-lattice Boltzmann method

We solve the flow of the incompressible Navier–Stokes equations with a common lattice Boltzmann technique [22]. We used a  $D3Q19$  model (19 discrete velocities in 3-D) and the usual BGK collision operator. While the [23] immersed boundary method has been implemented to impose the no-slip boundary condition on the surface of the particles, the [24,25] bounce-back method has been used to enforce the no-slip boundary condition for moving plates at the top and bottom. In the immersed boundary method, two sets of Lagrangian points, namely the marker and the reference points, are used to represent the surface of each particle. The fluid’s motion advects the marker points, while the reference points move as a rigid body. The difference in the positions between the marker and the reference points results in a Lagrangian force which is computed using an explicit spring force model [26]. By means of a linear interpolation scheme [1,26], these local Lagrangian forces are spread to the surrounding Eulerian fluid nodes by the [27] forcing scheme. The velocity at each Lagrangian boundary point is calculated by interpolating the fluid velocities at neighbouring nodes. We solve the linear and rotational motion of the particles by using explicit leapfrog integration of Newton’s equations. For more details, the reader is referred to our earlier paper [1].

Previously, we tested the accuracy of the implemented IB-LBM code by simulating the translation of a single rigid sphere at constant speed in the Newtonian liquid [1]. For the radius of  $R = 4$  lu, the effective size of the sphere (its hydrodynamic radius  $R_{hyd}$ ) increased by about 5% (4.2 lu) compared to the input radius  $R$ . It has been demonstrated by

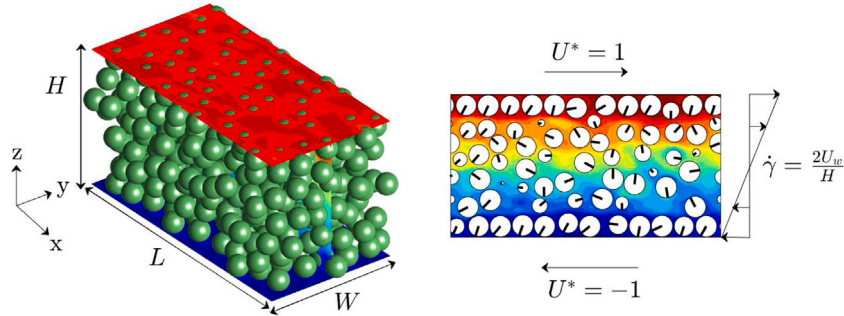


Fig. 1. Simulation geometry with particles suspended randomly in a Newtonian liquid subject to simple shear flow. The left panel shows the random location of the particles within the simulation box. The right panel shows 2-D cross-sections through the spheres that intersect the centre plane the simulation box. In both snapshots, the background colours indicate the  $x$  liquid velocity component normalised by the wall velocity  $U_w$ . (For interpretation of the references to colour in this figure legend, the reader is referred to the web version of this article.)

several authors [28,29] that the exact location of the no-slip condition differs from the “input” radius on the order of 0.2 to 1 lu. For particles with large input radii, the variation in the effective radius of this order is not significant [30]; however, we require a calibrated radius. This calibrated radius is used for the force calculation, solids volume fraction, and particle Reynolds number  $Re_p = \dot{\gamma} R_{hyd}^2 / \nu$  because it gives the effective position of the no-slip boundary. We perform the calibration under the conditions (low Reynolds number and a large domain) for which the equation for the force on a sphere (Stokes drag force) is valid.

Corrections to the fluid inside the sphere are not taken into account in any of the simulations discussed in this paper, and particles with densities twice that of the fluid density are simulated. The fluid density  $\rho_f$  is equal one (in lattice units), and the solid density is effectively  $\rho_s = \rho_p + \rho_f$ , where  $\rho_p$  is the additional density of the solid [28]. All simulations use  $\rho_p = 1$ , and it follows that the density ratio  $\sigma = \rho_s / \rho_f = 2$ .

### 3.2. Sub-grid scale lubrication corrections

The main difference between the suspension simulations described in this paper and our previous study [1] is that we now include sub-grid scale corrections for the unresolved normal and tangential lubrication forces and torques between particles. This is required because as soon as the gap between the surfaces of two spheres (or between the sphere and the wall) approaches the resolution of the simulation grid, the LB simulation will no longer accurately resolve the flow accurately in the gap. To improve the calculation of the forces and torques on the particles, we explicitly include lubrication corrections to account for sub-grid scale details of the flow. The expression for the leading order normal lubrication correction (NLC) on particle  $p$  due to relative translation of the spheres  $p$  and  $q$  along the line connecting the centres of the spheres is given by [20,30]

$$\mathbf{F}_p^{n,lub} = 6\pi\mu R_{hyd}^2 \frac{\alpha^2}{(1+\alpha)^2} \left( \frac{1}{h} - \frac{1}{h_o^n} \right) \mathbf{U}_n. \quad (1)$$

The superscript  $n$  denotes normal. For a monodisperse suspension, the ratio of the radii of spheres  $p$  and  $q$  is  $\alpha = R_{hyd}^q / R_{hyd}^p = 1$  and  $h = |\mathbf{x}_q - \mathbf{x}_p| - 2R_{hyd}$  is the gap between particles, where  $\mathbf{x}_p$  and  $\mathbf{x}_q$  are the centres of the spheres. The normal velocity  $\mathbf{U}_n = (\mathbf{U}_{pq} \cdot \hat{\mathbf{n}}_{pq}) \hat{\mathbf{n}}_{pq}$ , where  $\mathbf{U}_{pq} = \mathbf{u}_q - \mathbf{u}_p$  is the relative translational speed and  $\hat{\mathbf{n}}_{pq} = \frac{\mathbf{x}_q - \mathbf{x}_p}{\|\mathbf{x}_q - \mathbf{x}_p\|}$  is the unit vector that points from the centre of sphere  $p$  to the centre of sphere  $q$ .

The above Eq. (1) expresses the additional lubrication force that is needed to compensate for lack of resolution at small gap sizes. The lubrication expressions for the total lubrication forces are derived for Stokes flow and small film thickness (relative to particle radius). The particle Reynolds number is based on the characteristic velocity scale  $\dot{\gamma} R$  and length scale  $R$ . The approach speeds between particles

in suspensions are lower than this characteristic velocity, and the film thickness is smaller than the radius. Therefore, the film Reynolds number is smaller than the particle Reynolds number (0.105 to 0.529) which justifies the use of lubrication corrections.

The equations for computing the tangential lubrication force correction on the  $p$ th particle due to relative translation and rotation of the sphere perpendicular to the centreline are [18,20]

$$\mathbf{F}_p^{t,lub} = 6\pi\mu R_{hyd} \left[ \frac{4\alpha(2+\alpha+2\alpha^2)}{15(1+\alpha)^3} \ln \left( \frac{h}{h_o^t} \right) \right] \mathbf{U}_t, \quad (2a)$$

$$\mathbf{F}_p^{r,lub} = 6\pi\mu R_{hyd}^2 \left[ \frac{2\alpha^2}{15(1+\alpha)^2} \ln \left( \frac{h}{h_o^r} \right) \right] (\boldsymbol{\omega}^F \times \hat{\mathbf{n}}_{pq}). \quad (2b)$$

The superscripts  $t$  and  $r$  denote translation and rotation.  $\mathbf{U}_t = \mathbf{U}_{pq} - \mathbf{U}_n$  and  $\boldsymbol{\omega}^F = \boldsymbol{\omega}_{pq} + 4\alpha^{-1}\boldsymbol{\omega}_p + 4\alpha\boldsymbol{\omega}_q$  (where  $\boldsymbol{\omega}_{pq} = \boldsymbol{\omega}_p + \boldsymbol{\omega}_q$ ) are the relative tangential translational and rotational speeds. The translational and rotational lubrication cutoffs below which the corrections are applied are  $h_o^t$  and  $h_o^r$ , respectively. The lubrication torques due to the translation and rotation of the spheres are given by

$$\mathbf{T}_p^{t,lub} = 8\pi\mu R_{hyd}^2 \left[ \frac{\alpha(4+\alpha)}{10(1+\alpha)^2} \ln \left( \frac{h}{h_o^t} \right) \right] (\hat{\mathbf{n}}_{pq} \times \mathbf{U}_{pq}), \quad (3a)$$

$$\mathbf{T}_p^{r,lub} = 8\pi\mu R_{hyd}^3 \left[ \frac{2\alpha}{5(1+\alpha)} \ln \left( \frac{h}{h_o^r} \right) \right] \boldsymbol{\omega}^T, \quad (3b)$$

where  $\boldsymbol{\omega}^T = \left( \boldsymbol{\omega}_p + \frac{\alpha\boldsymbol{\omega}_q}{4} \right) - \left[ \left( \boldsymbol{\omega}_p + \frac{\alpha\boldsymbol{\omega}_q}{4} \right) \cdot \hat{\mathbf{n}}_{pq} \right] \hat{\mathbf{n}}_{pq}$ . The normal and tangential lubrication thresholds are estimated to be  $h_o^n / R_{hyd} = 0.72$  and  $h_o^t / R_{hyd} = h_o^r / R_{hyd} = 0.1$ , respectively. These values are computed from benchmark simulations of steady translation and rotation of rigid spheres with an input radius of  $R = 4$  lu at varying interparticle gaps, ensuring that the force and torque on the spheres is accurate in the limit  $h \rightarrow 0$ . We neither saturate the lubrication forces at small gap sizes nor introduce additional repulsive forces in the simulations to prevent overlap because for the cases considered, the divergence of the lubrication (correction) force with decreasing gap size is sufficient to prevent overlap.

The forces and torques on the  $q$ th particle can simply be written as  $\mathbf{F}_q = -\mathbf{F}_p$  and  $\mathbf{T}_q = \mathbf{T}_p$ . By taking the limit  $\alpha \rightarrow \infty$  in Eqs. (1) through (3b) and replacing  $q$  with  $w$  to denote a wall, one can derive the equations for the lubrication forces on a particle near either wall (equations are given in Appendix A). These wall contributions are added with the above equations to obtain the total (lubrication correction) forces and torques as

$$\mathbf{F}_p^{lub} = \mathbf{F}_p^{n,lub} + \mathbf{F}_p^{t,lub} + \mathbf{F}_p^{r,lub} + \mathbf{F}_p^{w,lub}, \quad (4a)$$

$$\mathbf{T}_p^{lub} = \mathbf{T}_p^{t,lub} + \mathbf{T}_p^{r,lub} + \mathbf{T}_p^{w,lub}, \quad (4b)$$

where  $\mathbf{F}_p^{w,lub}$  and  $\mathbf{T}_p^{w,lub}$  are the particle–wall lubrication force and torque corrections.

### 3.3. Particle motion

The integration of particle motion uses smaller time steps than the LBM flow solver. We ensure the stability of the integration of the explicit leapfrog scheme by using  $n_{tp}$  equal sub-time steps for every fluid time step. For  $\phi_v$  up to 40%, a constant number of sub-time steps was used throughout the simulation, and the required value of  $n_{tp}$  that is needed to ensure stability increases with increasing  $\phi_v$  and  $Re_p$ . To assess the effect of the number of sub-time steps, we considered two simulations at  $\phi_v = 17$  and 25% with  $Re_p = 0.32$ . While the difference in the apparent viscosity at 17% solids was 0.02% when the number of sub-time steps increased from 50 to 100, the difference was 0.14% for 25% solids when using 70 and 150 sub-time steps, respectively. This shows that the viscosities are therefore not sensitive to the number of sub-time steps.

We employed an adaptive time-stepping scheme for  $\phi_v = 47\%$ . When overlap between two particles or between a particle and a wall is detected, the integration of the particle motion is successively recalculated with double the number of sub-time steps until the overlap is no longer detected. In the next fluid time step, integration is first attempted with half the number of sub-time steps that was used for the previous fluid time step. In this way, the algorithm uses larger time steps for the particle motion when this is sufficient to resolve the interactions. In the simulations with 47% solids, the typical number of sub-time steps was 512. Using this adaptive time-stepping approach, we were able to simulate suspensions up to  $Re_p = 0.211$ , and the integration of particle motion is the bottleneck in the computational algorithm. For higher Reynolds numbers, the algorithm demanded impractically high numbers of sub-time steps (on the order of  $10^5$ ) to prevent overlap, and this was insufficient to prevent instability.

The computation of interparticle interaction forces is accelerated by the use of a binning algorithm instead of checking all pairs of particles to find those that are sufficiently close to applying lubrication corrections. The simulation domain is divided into a grid, and all particles are assigned to a cell within this grid. The algorithm then compares only the positions of particles that are in adjacent cells. With this algorithm, the suspension simulations were approximately seven times faster than with the less-efficient alternative.

The overall algorithm of IB-LBM with lubrication force computations is summarised as follows: at  $t = t_o$ , the fluid velocities and densities, as well as particle velocities and positions, are specified. For  $n_{tp}$  equal sub-time steps (constant or adaptive depending on the concentration of solids), the lubrication force and torque corrections are computed by employing the previously described binning algorithm. The velocity (translational and rotational) and the position of the particles is updated. The immersed boundary method is used to apply a no-slip condition on the surfaces of the particles: first, the Lagrangian force on the boundary points is spread to the neighbouring fluid nodes, and the velocity of each boundary points is obtained through interpolation of the fluid velocity on the neighbouring nodes. Finally, the flow field is solved using the LBM with the body forces specified by the immersed boundary method and the loop is executed until  $t = t_n$  (end of the simulation).

### 3.4. Relative apparent viscosity

The relative apparent viscosity of the suspension is determined as the sum of the resolved fluid shear stress and unresolved lubrication correction for particle–wall interactions. First, we evaluate the local fluid shear stress on every lattice node adjacent to the sheared walls (top and bottom) as

$$\tau_w^{LB} = \mu \frac{U_x - U_w}{\Delta y} \quad (5)$$

where  $\Delta y = 0.5$  lu is the distance between the wall and the neighbouring fluid node and  $\mu$  is the dynamic viscosity of the fluid. The

superscript *LB* denotes the resolved fluid contribution to the shear stress on either wall  $w$ . These local shear stresses are averaged across the  $x - y$  cross-sectional plane to obtain the total fluid shear stress. In the simulations with tangential lubrication correction (NTLC), the additional stress,  $\tau_w^{lub}$ , due to translation and rotation of particles near the walls is  $\frac{1}{LW} [\sum \mathbf{F}_p^{u,l} + \sum \mathbf{F}_p^{u,r}]$  (where  $\mathbf{F}_p^{u,l}$  and  $\mathbf{F}_p^{u,r}$  are the (lubrication correction) forces on particles — see Appendix A for equations). These contributions are added to Eq. (5) and the overall stress on the suspension and therefore the relative apparent viscosity is obtained as

$$\eta_r = \frac{\langle \tau_w^{LB} \rangle + \tau_w^{lub}}{\mu \dot{\gamma}} \quad (6)$$

In this equation,  $\langle \rangle$  denotes the average over the  $x - y$  cross-sectional area.

## 4. Three-dimensional simulations of suspensions

Three-dimensional simulations of dense monodisperse suspensions have been performed under simple shear flow. In these simulations, the solids volume fraction was varied between 6% and 47% and the particle Reynolds number between 0.105 and 0.529. Several different approaches have been taken to specify the initial positions of the spheres over the range of  $\phi_v$ . The specifics of these methods are set out in Appendix B. The liquid kinematic viscosity  $\nu = 1/30$  lu<sup>2</sup>/ts. Explicit NTLs were included to account for sub-grid scale details of the flow between solid surfaces. Simulations of dense suspensions (that is,  $\phi_v \geq 25\%$ ) ran on ICHEC (Irish Centre for High-End Computing) machines with  $2 \times 20$  core 2.4 GHz Intel Xeon Gold 6148 (Skylake) processors with 192 GB RAM. Local computing resources with 4 core Intel i7-6700 processor of 64 GB RAM were used to simulated dilute suspensions ( $\phi_v < 25\%$ ). In Section 4.1, we first discuss the rheology of suspensions at constant shear rates. Then we move on to address the transient rheology of suspensions due to flow reversals (in Section 4.2) and instantaneous shifts in the shear rate magnitude (in Section 4.3).

### 4.1. Steady-state rheology

For one set of randomly drawn particles (denoted as set 1), the evolution over time of apparent viscosities calculated from the stresses on the top and bottom walls under constant shear is presented in Fig. 2. The solids volume fractions were  $\phi_v = 6, 30, 38,$  and 47%, respectively, and  $Re_p = 0.105$ . The suspensions were sheared up to  $\dot{\gamma}t = 100$ . The figures display the individual contribution of resolved (by LBM), unresolved (modelled by NTLC), and the sum of both resolved and unresolved wall shear stresses (expressed as the implied relative apparent viscosity  $\eta_r$ ). Simulations with only NLCs for the above specified concentrations of solids have also been performed under simple shear flow, and a sample evolution of viscosity at 47% solids is shown in Fig. 2. Since the simulations with only NLC under-predict the viscosity of the suspension (as seen from the purple and orange dotted lines in Fig. 2), the inclusion of tangential lubrication corrections is necessary.

At  $\phi_v = 47\%$ , from Fig. 2, we can see that the viscosities computed from the (resolved) fluid stress (that is, dash-dot black and magenta lines) first increase up to  $\dot{\gamma}t \approx 5$  and then decrease before they start to stabilise after  $\dot{\gamma}t \approx 10$ . On the contrary, the viscosities computed from the (unresolved) lubrication stress (that is, dashed green and brown lines) are negligible until  $\dot{\gamma}t \approx 5$  due to the initial gap between the particles and either wall. Once the initial packing structure breaks, some particles approach to within the cutoff distance from the walls, and the lubrication stress rises rapidly to  $\dot{\gamma}t \approx 20$  and then stabilises. The sums of resolved and unresolved stresses, i.e., the (total) apparent viscosity of the suspension, are shown with blue and red lines. The smaller figures on the top panel of Fig. 2 display the evolution of relative apparent viscosity for several lower volume fractions ranging from 6 (top-left) to 38% (top-right). In the case of dilute suspensions (that is,  $\phi_v = 6\%$ ), we can see that the lubrication stress is negligible

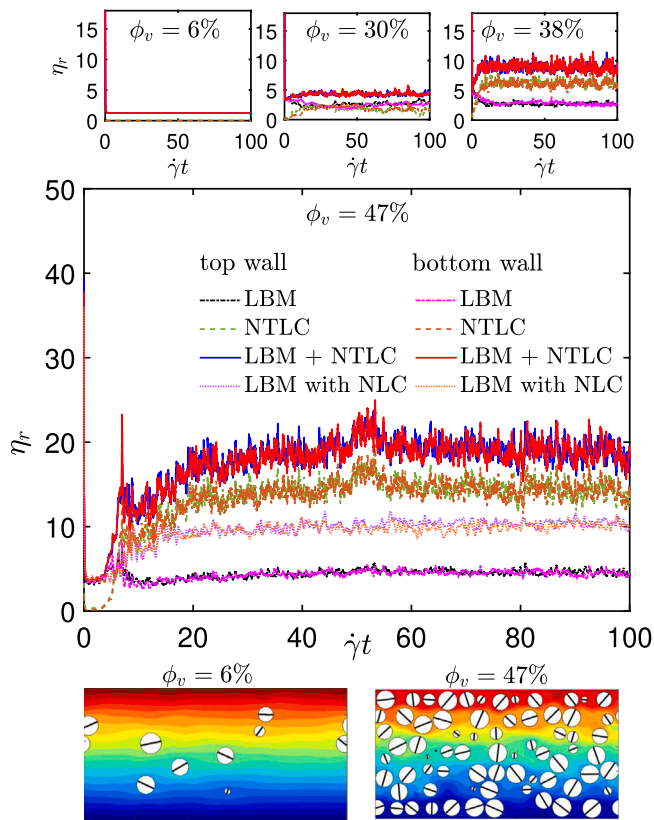


**Fig. 2.** Evolution of the relative apparent viscosity of a suspension at  $\phi_v = 47\%$  and  $Re_p = 0.105$  as a function of time ( $\dot{\gamma}t$ ) calculated from the stresses on the top and bottom walls. The Individual contributions of resolved (LBM) and unresolved (NTLC) shear stresses (expressed as the implied relative apparent viscosity) as well as their sum (LBM + NTLC) are shown. The dotted purple and orange lines indicate the simulation viscosity obtained by including the contribution of only NLC. Figures along the top show the evolution of  $\eta_r$  for  $\phi_v = 6, 30$ , and  $38\%$  with NTLCs, respectively. The images below show 2-D cross-sections through the simulation domains  $\phi_v = 6$  (left) and  $47\%$  (right) at  $\dot{\gamma}t = 50$ . (For interpretation of the references to colour in this figure legend, the reader is referred to the web version of this article.)

relative to the fluid stress. As the suspension becomes more dense, the number of particles adjacent to the wall increases (see the 2-D cross-sections at the bottom of Fig. 2) and the unresolved stresses surpass the resolved fluid stress; they are comparable in magnitude when the solids volume fraction is 30%.

Since the evolution of relative apparent viscosities determined from shear stress on either wall follows a similar trend, the average of top and bottom wall viscosities (denoted as  $\bar{\eta}_r = (\eta_r^t + \eta_r^b)/2$ , where the superscripts  $t$  and  $b$  denote top and bottom, respectively) is used in all subsequent discussions. While we see in Fig. 2 that the viscosity fluctuates throughout the simulations, the steady viscosity of the suspension is determined by averaging the variations over an interval of steady fluctuations. Since the suspensions were sheared up to  $\dot{\gamma}t = 100$ , based on Fig. 2, we average the viscosities between 50 and 100. These time-averaged viscosities are denoted as  $\bar{\bar{\eta}}_r$  (note the double over bar).

The effect of particle concentration on the time-averaged viscosity is shown for one random draw (set 1) in the left panel of Fig. 3 together with a comparison of  $\bar{\bar{\eta}}_r$  for three additional random configurations for the highest solids concentration (47%). The right panel shows the effect of shear rate (particle Reynolds number) on  $\bar{\bar{\eta}}_r$  for two random sets. We first discuss the results in the left panel of Fig. 3, which shows a comparison of  $\bar{\bar{\eta}}_r$  computed from the present work (that is, LB simulations with NTLCs) with the correlation of Krieger and Dougherty [21] with the parameters  $B = 2.5$  and  $\phi_c = 0.60$ , experiments of Dbouk et al. [12], and LB simulations of Thorimbert et al. [8] and Srinivasan et al. [1] at  $Re_p = 0.1$  and  $0.55$ , respectively.

For dilute suspensions (that is,  $\phi_v < 17\%$ ), our viscosities (filled magenta triangles) agree with [21] and [8]. As the concentration of solids increases ( $\phi_v \geq 17\%$ ), we see that the computed viscosities diverge from the data reported by both [21] and [8], and approach the value of Dbouk et al. [12]. We consider two reasons why our data deviate from particularly those reported by Thorimbert et al. [8], viz. (a) grid resolution and (b) interparticle forcing scheme. On the one hand, in terms of the grid resolution, the ratio of lattice spacing to particle radius,  $\Delta x/R$ , used in the simulations of Thorimbert et al. [8] is 0.2, whereas it is 0.25 (with  $\Delta x = 1$  lu and  $R = 4$  lu) in the current simulation. Sample simulations of suspensions with double the resolution (i.e.,  $R = 8$  lu such that  $\Delta x/R = 0.125$ ) showed that for  $\phi_v \geq 40\%$ , the viscosities decrease by approximately 16% and agree closely with [8]. On the other hand, analysing the results in terms of interparticle force models, the simulations of Thorimbert et al. [8] used a spring-like repulsive force for sub-grid scale interactions, and the details of the hydrodynamic lubrication correction over short distances were not modelled. In our current simulations with hydrodynamic lubrication forces, the contribution of tangential stress is shown to be prominent (see Fig. 2), and therefore the relative apparent viscosity is higher.

Presented with filled and open diamonds are the results of our previous study [1] at  $Re_p = 0.55$ . In these simulations, we applied a spring force between the colliding particles to prevent overlap when the distance between any neighbouring particles is less than 1 lu. The filled diamonds are drawn at the volume fraction corresponding to the hydrodynamic radius  $R_{hyd} = 4.2$  lu, while the open diamonds are drawn at  $\phi_v$  calculated based on the spring radius  $R_{spring} = 4.5$  lu (which follows from the separation distance imposed by the repulsive spring force). Interestingly, we can see that our previous findings match with the [21] correlation if  $\phi_v$  was computed based on the spring radius. This effect is, however, not present in current simulations with NTLC.

Now we move on to address the effects of particle Reynolds number shown in the right panel of Fig. 3 on the time-averaged suspension viscosity. Two different sets of particle configurations were considered, namely set 1 (triangles) and set 2 (circles). We will first discuss the simulation results of set 1. In the regime of dilute suspensions (that is,  $\phi_v \leq 17\%$ ), it is evident that the influence of  $Re_p$  has no effect on  $\bar{\eta}_r$  (as the viscosity remains steady with increasing  $Re_p$ ). However, for  $\phi_v = 30$  and  $35\%$ , we see that the viscosity first decreases slightly with increasing  $Re_p$  up to 0.317. The viscosity then temporarily increases at  $Re_p = 0.423$  and decreases at  $Re_p = 0.529$ . In order to understand the reason for this temporary increase in the viscosity, we performed one additional simulation for both concentrations at  $Re_p = 0.423$  with a different collection of random particles (set 2). From the circles shown in green and black, we can see that the viscosity is lower than that of set 1 and follows a weak shear-thinning behaviour. This leads us to the conclusion that the higher viscosity value seen for set 1 is associated with the choice of random initial particle configuration.

In the case of solid concentrations at 40 and 47%, we were able to simulate suspensions up to  $Re_p = 0.317$  and  $0.211$ , respectively, with the current numerical scheme, before encountering instability in the integration of particle motion. At these high concentrations, the rheological behaviour of suspensions changes to weak shear-thickening ( $\phi_v > 40\%$ ). A similar transformation in rheology has also been observed in the transient simulations — details are given in the next section.

In all simulations presented so far, one random configuration (set 1) was chosen to analyse the steady-state rheology (for which the results agree with the literature — see Fig. 3). The effects of simulating suspensions with particles from multiple random sets (denoted as sets 2, 3, and 4, respectively) are now evaluated. Since the concentration of solids varies between 6 and 47%, we use these two extremes to investigate the sensitivity of different initial particle positions for one particle Reynolds number,  $Re_p = 0.105$ . The left panel of Fig. 4 shows the temporal

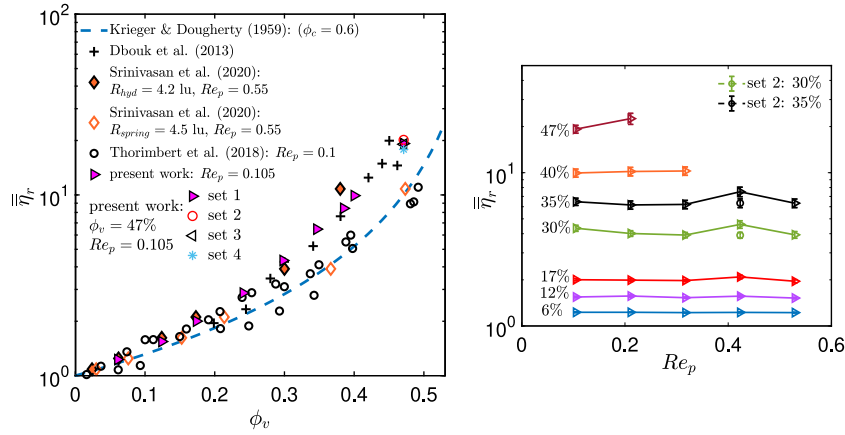


**Fig. 3.** Left panel: the time-averaged relative apparent viscosities of the present work (IB-LBM simulations with NTLC: filled magenta triangles) for varying solids volume fraction and  $Re_p = 0.105$  are compared with [21] (dashed line), [12] (pluses), [8] (open circles), and [1] (filled and open diamonds). For each solids fraction, data are shown for one random initial particle configuration; for 47% solids, data sets for three additional initial configurations are shown. The significance of using two types of diamonds to represent the results of Srinivasan et al. [1] is that  $\phi_v$  is determined on the basis of  $Re_{hyd}$  and  $Re_{spring}$  for the results in the filled and opened diamonds, respectively. Right panel: all symbols correspond to IB-LBM simulations with NTLCs. For the set 1 particle configurations (right-pointing triangles), the effect of  $Re_p$  on the time-averaged  $\bar{\eta}_r$  is shown for  $\phi_v$  between 6 and 47%. Circles reveal the additional simulation viscosity obtained for the set 2 particle configurations at  $Re_p = 0.423$  and  $\phi_v = 30$  and 35%, respectively. (For interpretation of the references to colour in this figure legend, the reader is referred to the web version of this article.)

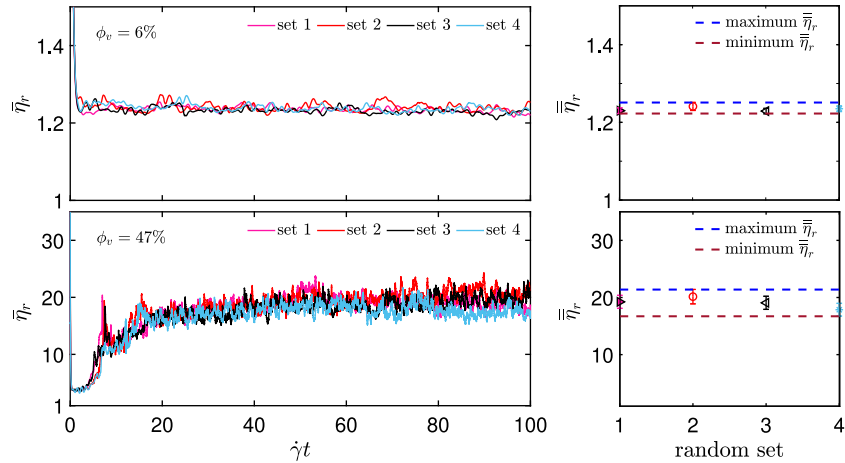


**Fig. 4.** The evolution of the average (of top and bottom wall) relative apparent viscosity,  $\bar{\eta}_r$ , for four different random configurations at  $\phi_v = 6$  and 47%, and  $Re_p = 0.105$  is shown in the left panel. The mean viscosity values differ depending on the configuration, as shown in the right panel, where  $\bar{\eta}_r$  is  $\bar{\eta}_r$  averaged over  $50 \leq \dot{\gamma}t \leq 100$ . The error bars show the standard deviation, and the maximum and minimum values of  $\bar{\eta}_r$  are calculated by adding and subtracting the standard deviation from the highest and the lowest mean values. (For interpretation of the references to colour in this figure legend, the reader is referred to the web version of this article.)

evolution of  $\bar{\eta}_r$  for all four randomly placed particles, whereas the right panel shows the time-averaged viscosity. Like previously, the viscosities were averaged over  $50 \leq \dot{\gamma}t \leq 100$  to obtain  $\bar{\eta}_r$ . For 6% solids, random packing was used, while a cubic packing with random perturbations was used for 47% solids.

From the time evolution plot, it is evident that, in both cases, the details of the fluctuations in viscosity are different for each random configuration; nonetheless, the suspensions attain statistical steadiness once the initial packing arrangement collapses. The number of interactions between the particles (and between the particles and walls) increases as the solids loading increases, and hence the frequency of fluctuation increases for  $\phi_v = 47\%$ . The average viscosity, as well as the maximum and minimum values of these fluctuations, are presented in the right panel as symbols and dashed blue and brown lines. The maximum  $\bar{\eta}_r$  is calculated by adding the standard deviation to the highest (of all four configurations) average value, while the minimum  $\bar{\eta}_r$  is calculated by subtracting the standard deviation from the lowest (of all four configurations) average value. For dilute suspensions, the standard deviations are meagre, whereas for 47% solids, simulations with set 2 and set 4 particles provide the highest (20.15) and the

lowest (17.86) average viscosity values, respectively. The results are presented in Fig. 3, and it is evident that all values nearly coincide with [12], implying that our conclusions are not sensitive to the choice of the random initial configuration. Therefore, we discuss the results of transient simulations (both shear reversals and step changes in the magnitude of shear rates) for one configuration (set 1).

#### 4.2. Effects of flow reversal

In the steady-state rheology calculations, the shear rate was constant throughout the simulation. However, in some situations, such as disrupted flow due to obstructions and bends in pipes and valves, the shear rate's direction and magnitude can vary in time and space. It is, therefore, essential to learn how the rheology and structure of suspensions may change under these conditions. In the sections that follow, we analyse the effects of reversing the shear flow direction instantaneously on (a) the suspension rheology and (b) the spatial distribution of particles. For a number of  $\phi_v$  values ranging from 10 to 40% and two Reynolds numbers,  $Re_p = 0.105$  (solid blue lines) and 0.317 (solid green lines), numerical results of the shear reversal simulations are discussed.

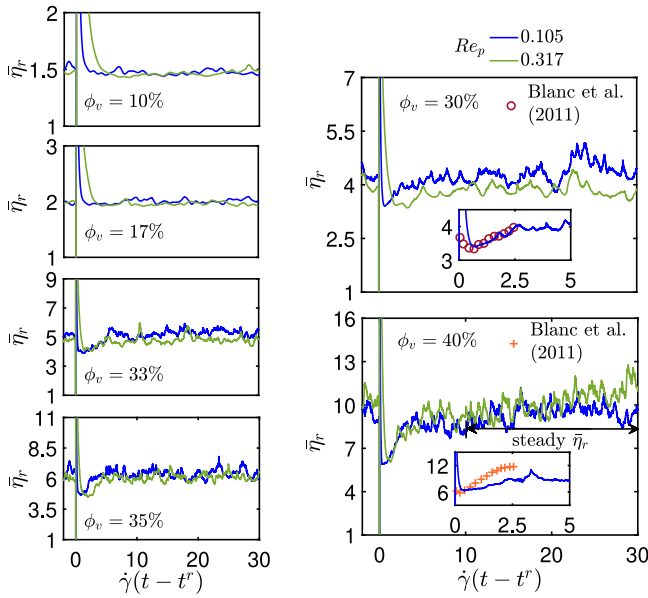


**Fig. 5.** Average relative apparent viscosity as a function of accumulated strain after flow reversal at  $Re_p = 0.105$  (solid blue lines) and  $0.317$  (solid green lines). The concentration of solids varies from 10 to 40%. Insets in the right panel show a comparison of the numerical results obtained by IB-LBM simulation for  $\phi_v = 30$  and  $40\%$  at  $Re_p = 0.105$  with the experimental results (symbols) of Blanc et al. [16] under Stokes condition ( $Re_p \sim 10^{-9} - 10^{-7}$ ). (For interpretation of the references to colour in this figure legend, the reader is referred to the web version of this article.)

#### 4.2.1. Rheology

Shown in Fig. 5 is the average relative apparent viscosity as a function of the accumulated strain after the time of the reversal ( $t'$ ). The constant shear simulation shows that following the initial increase from the minimum (see Fig. 2), the apparent viscosity achieves statistical steadiness after about 20 strain times. Therefore, in all of these simulations, the suspension was first sheared up to  $\dot{\gamma}t' = 30$  (except at  $\phi_v = 40\%$ , where  $\dot{\gamma}t' = 40$  to ensure steady fluctuations) in one direction. After reversing the direction of shear flow ( $t \geq t'$ ), all the simulations ran up to  $\dot{\gamma}(t-t') = 30$ , and the steady viscosity is calculated by averaging the value between  $10 \leq \dot{\gamma}(t-t') \leq 30$  (as shown as arrow in bottom right panel of Fig. 5) because the suspensions regain their equilibrium configuration sooner than starting from a random cubic packing. At 40% solids, from the green line ( $Re_p = 0.317$ ), at the end of the simulation ( $\dot{\gamma}(t-t') > 28$ ), although one might argue that the trend appears to be increasing, we interpret this to be a temporary fluctuation of the apparent viscosity (which is related to temporary collisions between particles and particles and walls). A similar behaviour can also be seen in Fig. 2 at  $\dot{\gamma}t \approx 50$ , where the apparent viscosity suddenly increases, and then descends to the previous range.

Consistent with our observation from the constant shear simulations (see right panel of Fig. 3), even after flow reversal, we can see in Fig. 5 that the rheology of the suspension varies from weak shear-thinning (at  $\phi_v = 30$  and  $33\%$ ) to weak shear-thickening (at 40% solids); at  $\phi_v = 35\%$ , the viscosities are comparable. These changes in the rheological behaviour of suspensions are related to the slower rotation of particles at high volume fractions [1]. In dilute suspensions, the particles rotate at half the imposed shear rate (that is,  $\omega_p = \dot{\gamma}/2$ ); however, as the concentration of solids increases, the (temporary) clustering of particles increases. Such clusters may occupy most of the space in the wall-normal direction, and they rotate slower than individual particles. An example of the distribution of clusters is presented in Section 4.2.2 — see Fig. 9. Overall, cluster rotations have a major impact not only on the steady viscosity [1] but also on the transient viscosity.

At  $t = t'$ , we switch the direction of the walls instantaneously (while maintained the same speed), and the shear stress on the walls

(and therefore the relative apparent viscosity) instantly increases from its previous steady value (that is,  $\dot{\gamma}(t-t') < 0$ ) and then decreases as the boundary layer develops. In the case of low concentrations of solids (10 and 17%), the viscosity tends to decrease until the previous steady-state value is reached. With an increase in the concentration of solids ( $\phi_v \geq 30\%$ ), the viscosity first decreases to a minimum and then increases to a steady value. The magnitude of the temporary decrease in the viscosity increases with increasing solids volume fraction.

The insets in the figures on the right panel of Fig. 5 present a comparison of the simulated viscosities ( $Re_p = 0.105$ ) with the experimental values of Blanc et al. [16] at Stokes flow condition ( $Re_p \sim 10^{-9} - 10^{-7} \ll 1$ ). At 30% solids, the minimum viscosity after shear reversal and the steady value are consistent with [16]. At the higher volume fraction (40% solids), the minimum simulation viscosity deviates from [16] by  $\approx 4\%$ . From a steady value of about 10 prior to the flow reversal, the viscosity after reversing the flow drops to a minimum of  $\approx 7$ . Though the steady structure of the particle arrangement is destroyed temporarily due to an instantaneous flow reversal, the structure eventually rebuilds and the relative apparent viscosity returns to 10 (average over  $10 \leq \dot{\gamma}(t-t') \leq 30$ ). Simulations with a different random initial particle configuration (set 2) were performed and the differences in the viscosity were found to be minor.

With an increase in the solids concentration, we observe a delay in the development of the suspension viscosity that decreases with increasing  $\phi_v$ . We analyse the reason for this delay by considering the development of the viscosity of the suspension over two time scales. The first of these scales is the viscous time scale based on the domain height, and the second is an advection time scale based on the mean centre–centre distance between particles. We first present in Fig. 6, a comparison of the wall shear stress (instantaneous average relative apparent viscosity) as a function of time scaled by the viscous time scale  $H^2/\nu$  for  $\phi_v$  between 10 and 40% and  $Re_p = 0.105$  and  $0.317$ . We can see that the minimum viscosities coincide for both  $Re_p$ , which indicates that the dynamics of the first stage (the attainment of the minimum viscosity) are determined by the viscous time scale. For 10 and 17% solids, the initial decreases in the viscosity of the suspension have similar slopes until becoming steady for  $(t-t')\nu/H^2 \geq 0.1$ . With increasing  $\phi_v$ , the slope of  $\bar{\eta}_r$  increases, and the time to reach the minimum viscosity decreases (relative to the viscous time scale) as the higher number of solids increases the apparent viscosity (and accelerates momentum transport).

Along with the simulation results, in Fig. 6, we also present the analytical solution [31] for the developing shear stress in the absence of particles (dashed magenta line). The slope from the LB simulation with  $\phi_v = 10\%$  matches with the analytical solution well during the initial development of the wall shear stress. Under the steady-state condition, the analytical relative apparent viscosity must be exactly equal to 1. The deviation of  $\bar{\eta}_r$  in the simulation for  $(t-t')\nu/H^2 > 0.1$  reflects the higher viscosity of a suspension with 10% solids.

For all dense suspensions ( $\phi_v \geq 30\%$ ) presented in Fig. 5, after the attainment of the minimum viscosity, the suspension slowly re-structures to a stable configuration. We remark here that the spatial arrangement of particles contributes to the relative apparent viscosity at higher solids fractions. This re-structuring of suspensions occurs over an advective timescale. Taking  $\dot{\gamma}R_{hyd}$  as the velocity scale and the mean centre–centre distance  $l = \sqrt[3]{V/N_p} = R_{hyd} \sqrt[3]{4\pi/(3\phi_v)}$  (where  $V$  is the volume of the simulation domain) as the length scale, we form the advective time scale  $l/(\dot{\gamma}R_{hyd})$ . Fig. 7 presents the development of  $\bar{\eta}_r$  as a function of time scaled by this advective time scale starting from rest with random particle positions (left panel) and after flow reversal (right panel). For this analysis, we consider solids volume fractions up to 47% and  $Re_p = 0.105$ . While the development of  $\bar{\eta}_r$  from rest follows a similar pattern for  $\phi_v$  up to 35%, the variations seen in the initial trends at higher concentrations ( $\phi_v = 40$  and 47%) are due to the use of a cubic packing (details are given in Appendix B). From the right panel of Fig. 7, it is evident that the relative apparent

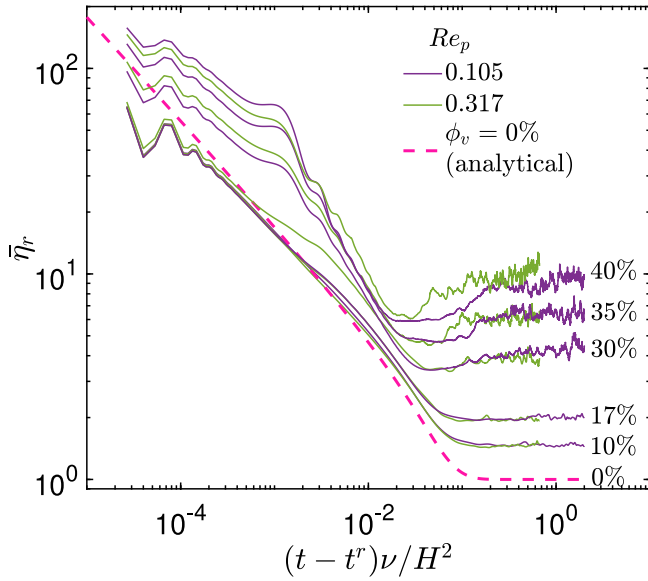


**Fig. 6.** Wall shear stress (expressed as the implied average relative apparent viscosity  $\bar{\eta}_r$ ) after shear reversal as a function of time scaled by the viscous time scale  $H^2/\nu$ . The solids volume fractions vary from 0% to 40% in the order of increasing viscosity, and  $Re_p = 0.105$  and  $0.317$ . The initial particle positions correspond to set 1 of Fig. 5. The dashed magenta line shows the analytical solution for  $\bar{\eta}_r$  in the absence of suspended particles ( $\phi_v = 0\%$ ). (For interpretation of the references to colour in this figure legend, the reader is referred to the web version of this article.)

viscosity evolves differently after flow reversals. In both panels, for all dense suspensions (that is,  $\phi_v \geq 30\%$ ), after the first increase from the minimum value, a steady viscosity is achieved between 2 and 4 advective time scales. Instead of defining the length scale based on mean centre–centre distance, one could use the gap size between adjacent particles (that is,  $l - 2R_{hyd}$ ). Using an advective timescale based on this length, the non-dimensional time for the suspension to re-structure to the equilibrium state increases with  $\phi_v$ .

#### 4.2.2. Structure

As mentioned earlier, flow reversal that can occur due to sudden change in the geometry of the transport line affects not only the rheology observed so far, but also the structural arrangement of the particles. Therefore, we study the spatial distribution of particles in two different ways, i.e. (a) study of the evolution of particle clusters and (b) pair distribution function. The purpose of the first analysis is to provide a qualitative description of the changes in structure after a reversal of the shear direction. In this analysis, we count the number of particles that are within a certain cutoff  $h_c$  (which we call the cluster cutoff).

The dependence of the number of clusters on the choice of cutoff value describes how the particles are distributed in space. The second analysis shows the pair distribution function at steady-state after shear reversal.

For the first analysis, a cluster is defined as a collection of two or more particles in which the gap between each particle and at least one other particle in the cluster is smaller than  $h_c^* = h_c/R_{hyd}$ . Presented in Fig. 8 are the comparisons of the evolution of both the number of clusters  $N_c$  (left vertical axis) and the average relative apparent viscosity  $\bar{\eta}_r$  (right vertical axis) after shear reversal as a function of time for several concentrations of solids. In order to illustrate the evolution of the suspension structure, we pick  $h_c^*$  to obtain approximately 20 clusters at steady-state after flow reversal for all concentrations. Comparing the evolution of the number of clusters and the relative apparent viscosity, we see that the time scales of these processes coincide during both the initial development and attainment of the steady value. For example, at 47% solids, both  $N_c$  and  $\bar{\eta}_r$  begin to stabilise after flow reversal, when  $\dot{\gamma}(t - t^r) \geq 5$ . In all dense suspensions ( $\phi_v \geq 33\%$ ), a temporary increase in the number of clusters is seen after flow reversal, with a maximum of approximately 50 clusters for all such suspensions. This increase is because the particles are temporarily loosened from their previous configuration (prior to flow reversal), causing the group of particles detected within the chosen cutoff to disintegrate into several groups of small clusters, thus increasing the overall cluster count.

A sample visualisation of the spatial distribution of clusters at the end of shear reversal ( $\dot{\gamma}(t - t^r) = 30$ ) is presented in Fig. 9. In each scenario, the number of particles in a cluster differs, and the particles with same colour indicate the group of clusters. As the concentration of solids increases, we can see that a cluster (coloured in transparent olive green) takes up the entire space along the wall-normal direction. For the same cluster threshold as used in illustrating the temporal evolution of  $N_c$  in Fig. 8, the number of clusters in the order of increasing  $\phi_v$  at  $\dot{\gamma}(t - t^r) = 30$  is 13, 14, 14, and 9, respectively. In Fig. 9, each of these clusters is coloured differently to show their spatial distribution.

Next, we interpret the spatial distribution of particles after flow reversal by calculating the average cluster size  $Q = N_p N_s / N_c^t$  where  $N_p$  is the number of particles and  $N_c^t$  is the total number of clusters (including all individual particles not within  $h_c^*$ ) observed over  $N_s$  simulation samples. The definition of  $Q$  is such that its value is between 1 and  $N_p$ . When  $Q = 1$  there are no clusters, and  $Q = N_p$  implies that all particles are counted as being in one cluster. The left panel of Fig. 10 shows the dependence of the average cluster size after flow reversal on the value of  $h_c^*$  for  $\phi_v = 10, 33, 40,$  and  $47\%$ . With an increase in  $\phi_v$ , for a fixed  $h_c^*$  the average cluster size increases because of the presence of more particles in a constant volume. While for 10% solids, the average cluster size at  $h_c^* = 0.119$  is  $\approx 1.2$ , for the same cluster threshold at 47% solids  $Q$  is  $\approx 244$ . For all  $\phi_v$ , the average cluster size plateaus to coincide with  $N_p$  when  $h_c^*$  surpasses a critical value. In this case, all particles are counted as being in a single cluster. For instance, at 47%

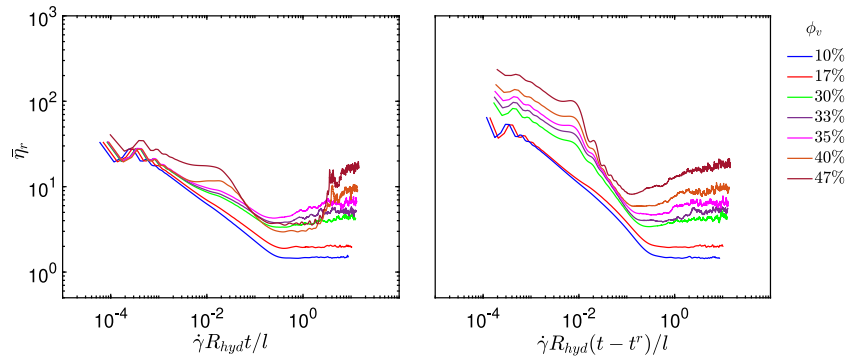


**Fig. 7.** Time-evolution of the wall shear stress (average relative apparent viscosity) of suspensions starting from rest with random particle configurations (left) and after shear reversal (right). Simulation time is scaled by the advective time scale,  $l/(\dot{\gamma}R_{hyd})$ , with  $l$  being the mean centre–centre distance. For all solids concentrations ( $10\% \leq \phi_v \leq 47\%$ ) the particle Reynolds number is 0.105.

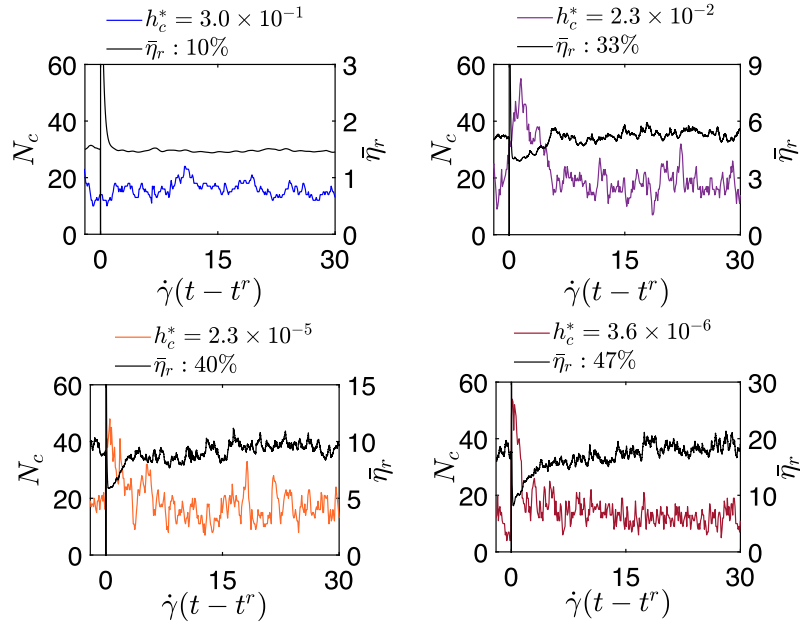


**Fig. 8.** The evolution of the number of clusters  $N_c$  (left vertical axis) and the relative apparent viscosity  $\bar{\eta}_r$  (right vertical axis) as a function of non-dimensional time  $\dot{\gamma}(t - t^r)$  after a reversal of the shear direction for several values of  $\phi_v$  at  $Re_p = 0.105$ . In all simulations,  $h_c^*$  was chosen to obtain  $\approx 20$  clusters at steady-state after flow reversal. (For interpretation of the references to colour in this figure legend, the reader is referred to the web version of this article.)

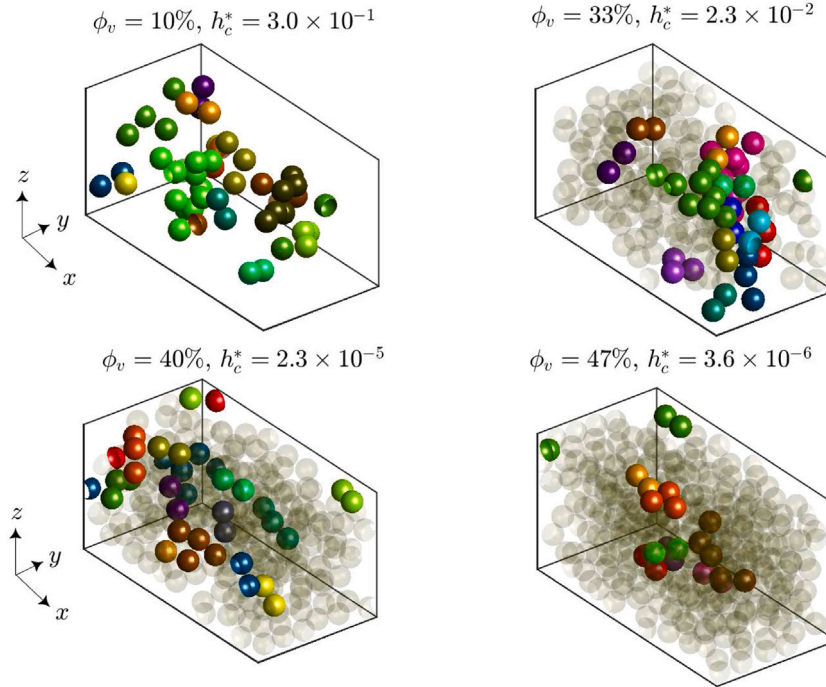


**Fig. 9.** The spatial distribution of particles with clusters (drawn in different colours) at the end of the simulation ( $\dot{\gamma}(t - t^r) = 30$ ) is shown for  $\phi_v = 10, 33, 40$ , and  $47\%$ . The transparent olive colour particles at  $\phi_v = 33, 40$ , and  $47\%$  are all in one cluster. The same cluster threshold as illustrated in Fig. 8 is used to demonstrate the distribution of clusters. The particle Reynolds number is  $Re_p = 0.015$ . (For interpretation of the references to colour in this figure legend, the reader is referred to the web version of this article.)

solids,  $Q = N_p = 432$  when  $h_c^* \geq 0.25$ . For  $h_c^* < 0.25$ , the average cluster size increases quickly with increasing  $h_c^*$ .

For the second analysis, we quantitatively interpret the structural arrangement of the particles in our suspensions using the pair distribution function  $g(r)$  [32]. For the collection of particles,  $g(r)$  is computed as

$$g(r) = \frac{V}{4\pi r^2 \delta r N_p^2} \sum_{p=1}^{N_p} \sum_{q=p}^{N_p} \Theta(|\mathbf{r}_{pq}| - r) \Theta(r + \delta r - |\mathbf{r}_{pq}|) \quad (7)$$

$$\Theta(X) = \begin{cases} 1, & X > 0 \\ 0, & X < 0 \end{cases} \quad (8)$$

where  $V$  is the volume of the simulation box,  $r$  is the distance from the centre of a particle,  $\delta r = 1$  is the thickness of the ring used for calculating  $g(r)$ ,  $|\mathbf{r}_{pq}|$  is the distance vector, and  $\Theta(X)$  is a step function. The pair distribution function provides information on the probability of finding a particle at a distance between  $r$  and  $r + \delta r$  of a reference

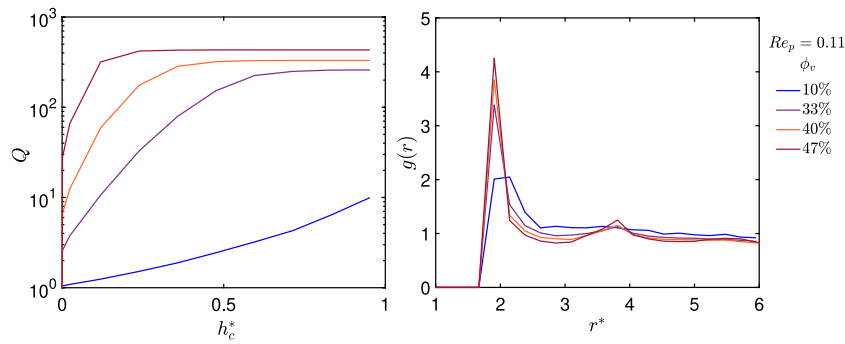


**Fig. 10.** Left panel: the dependence of the average cluster size  $Q$  on  $h_c^*$  for  $\phi_v = 10, 33, 40,$  and  $47\%$ . In order of increasing solids concentration, the total number of particles in each case is 85, 259, 330, and 432, respectively. Right panel: the pair distribution function  $g(r)$  for the same solids concentrations. For each  $\phi_v$ ,  $g(r)$  is averaged over the steady-state ( $20 \leq \dot{\gamma}(t-t') \leq 30$  sampled every 500 LB time steps) particle configurations observed after flow reversal.

particle. Since the simulation box is a cuboid (with  $W = L/2$ ), we consider  $r$  over the range  $1 \leq r \leq W/2$ . In the right panel of Fig. 10, we calculate  $g(r)$  for suspensions between 10 and 47% solids after shear reversal at  $Re_p = 0.105$ .  $g(r)$  is averaged over all steady-state particle configurations after flow reversal. The position of the first peak in the right panel of Fig. 10 shows how the distance between the particles decreases as the solids fraction increases. The second smaller peak in dense suspensions at about  $r^* = r/R_{hyd} = 3.7$  (also seen by Sierou and Brady [32]) shows the development of longer range structure in the suspension. For a further increase in  $r^* > 4$ , we do not observe any further peaks which suggests that the size of the structures is limited.

#### 4.3. Effects of step changes in the shear rate

We now study the transient behaviour of dense suspensions in response to step changes in the magnitude of the shear rate. For this purpose, we consider two solids fractions,  $\phi_v = 40$  and  $47\%$ . At 40% solids, we used the same initial cubic packing as previously (details are provided in Appendix B). In order to show trends more clearly, in Fig. 11,  $\bar{\eta}_r$  is obtained by averaging the results of simulations with two initial particle configurations. For 47% we use an initial particle configuration from the period of steady fluctuations shown in Fig. 2. The number of sub-time steps is constant for 40% solids, and it is determined by the requirements for the highest  $Re_p = 0.211$  to ensure stability throughout the simulations. The adaptive algorithm for the number of sub-time steps was used for 47% solids.

The left panel of Fig. 11 shows the evolution of the average relative apparent viscosity as a function of the accumulated strain  $\dot{\gamma}_o t$  starting from rest (where  $\dot{\gamma}_o$  is the initial shear rate that corresponds to  $Re_p = 0.105$ ). The shear rate is increased by a single step up to  $Re_p = 0.211$  (red lines) at  $\dot{\gamma}_o t = 18.5$ . The shear rate then remains steady until  $\dot{\gamma}_o t = 24.2$ . For comparison, we also show the data for simulations with a constant shear rate ( $Re_p = 0.105$ ; green lines). Considering the range of the fluctuations, we conclude that the apparent viscosities after shearing at  $Re_p = 0.211$  are the same as with  $Re_p = 0.105$  for both solids fractions; the average relative viscosities are 10 ( $\phi_v = 40\%$ ) and 17 ( $\phi_v = 47\%$ ), respectively.

After shearing the suspensions at  $Re_p = 0.211$ , we consider how the viscosity of the suspensions evolves when the shear rate is restored to  $Re_p = 0.105$  (right panel of Fig. 11). The relative viscosity of the lower solid fraction (40%) shows no significant history effect, returning to  $\approx 10$ . For  $\phi_v = 47\%$ , however, temporary shear at a higher speed results in an increase in the apparent viscosity when the shear rate returns to its previous value. The viscosity increases by approximately 16% (from an average of 17 in the high shear regime to slightly over 20 in the low shear regime). The right panel of Fig. 11 also includes one additional case (black lines): instead of continuing from the complete simulation state of the red case at the end of shearing at  $Re_p = 0.211$ , the fluid and particle velocities are reset to zero. The only history

that is retained is the positions of the particles but not their speeds or the motion of the interstitial liquid. The average relative apparent viscosities ( $28 \leq \dot{\gamma}t \leq 30$ ) in these situations are within 2 and 6% of the constant shear simulations at  $\phi_v = 40$  and  $47\%$  solids, respectively, implying that stopping and resuming the flow will negate the effect of temporary shear at a higher rate. From these observations, we conclude that the rheology of suspensions depends not only on the positions of the particles but also the flow history of the interstitial fluid.

#### 5. Conclusions

Three-dimensional simulations of suspensions have been performed using an immersed boundary-lattice Boltzmann method for Reynolds numbers in the range  $0.105 \leq Re_p \leq 0.529$  and solids volume fractions from 5 to 47%. The simulations included corrections for unresolved lubrication forces and torques over sub-grid scale distances. Up to  $\phi_v = 47\%$ , the relative apparent viscosity of suspensions showed good agreement with the experimental data of Dbouk et al. [12] but deviate from the simulations of Thorimbert et al. [8]. This difference is attributed to the grid resolution of our simulations as well as the incorporation of tangential lubrication corrections during sub-grid scale interactions. As the concentration of solids increases ( $\phi_v \geq 30\%$ ), it was found that the unresolved tangential stress due to the translation and rotation of particles near the walls contributes significantly to the total stress on the walls and therefore to the apparent viscosity. Overall, the viscosity of the suspension showed no dependence on the Reynolds number for  $\phi_v \leq 17\%$ , weak shear-thinning at 30 and 35% solids, and weak shear-thickening at  $\phi_v > 40\%$ .

Simulations of suspensions submitted to an instantaneous flow reversal were performed for solid fractions between 10 and 47% with  $Re_p = 0.105$  and  $0.317$ ; for 47% of solids, simulations were conducted for  $Re_p = 0.105$  and  $0.211$ , respectively. The initial development of the wall shear stress after reversing the flow follows a viscous time scale. Dilute suspensions ( $\phi_v \leq 17\%$ ) obey the trend of pure Newtonian liquid ( $\phi_v = 0\%$ ). At higher volume fractions, minimum shear stress is observed until the shear stress increases to a steady value that depends on the imposed shear rate. This minimum stress is the same for both  $Re_p$ . As  $\phi_v$  increases, the mean centre-centre distance between the particles decreases, and an advective timescale based on this mean distance governs the dynamics of the re-structuring of the suspension towards a steady viscosity. Although the structure of the particle assembly collapses after flow reversal, the previous structure is then rebuilt over this advective time scale.

In the case of  $\phi_v$  between 10 and 47%, the time scales of the evolution of both the structures and the relative apparent viscosity were found to coincide. The pair distribution function of these suspensions has shown the existence of particle structures that facilitate higher momentum transport and therefore higher relative apparent viscosity in such dense suspensions.

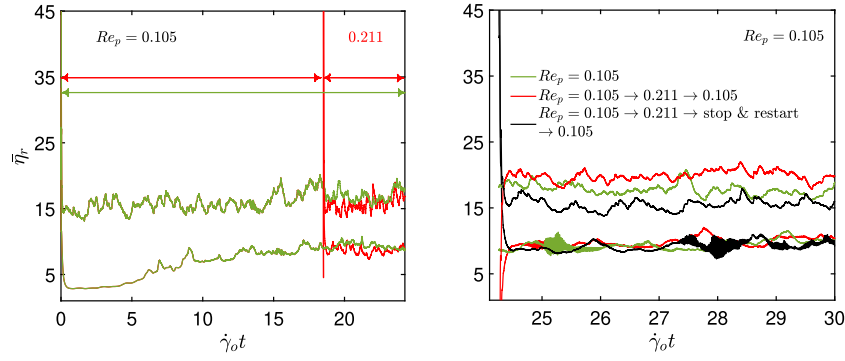


**Fig. 11.** Average relative apparent viscosity as a function of time for suspensions with  $\phi_v = 40\%$  (bottom set; lower viscosity) and  $47\%$  (top set; higher viscosity). In the left panel, the coloured arrows at the top show the duration of the different shear rates for each case. The right panel demonstrates the evolution of the average viscosity after bringing the shear rate down to its original value (that is,  $Re_p = 0.105$ ) from the previous high shear regime. The black lines in the right panel show the effect of stopping the motion of the fluid and particle at  $\dot{\gamma}_o t = 24.2$  and restarting the flow from the location of the particle at that time. (For interpretation of the references to colour in this figure legend, the reader is referred to the web version of this article.)

At the highest solids fraction we considered ( $\phi_v = 47\%$ ), simulations with step increases in the magnitude (but not the direction) of the shear rate showed a 16% higher viscosity when the shear rate returned to its initial value. At low fractions ( $\phi_v = 40\%$ ), history effects on the viscosity of the suspension were negligible. The memory effect seen at  $\phi_v = 47\%$  was removed when motion of the fluid and particles was stopped before shearing again at the initial rate.

Our next goal is to investigate consequences of including additional sub-grid scale non-hydrodynamic forces on both the steady-state and transient rheology of dense suspensions. To this end, we will study the effects of electrostatic repulsion and van der Waals attraction forces as a function of particle Reynolds number and solids volume fraction.

### CRediT authorship contribution statement

**Sudharsan Srinivasan:** Conceptualisation, Formal analysis, Investigation, Methodology, Software, Validation, Visualization, Writing – original draft, Writing – review & editing. **Harry E.A. Van den Akker:** Conceptualisation, Formal analysis, Funding acquisition, Methodology, Project administration, Supervision, Validation, Writing – review & editing. **Orest Shardt:** Conceptualisation, Formal analysis, Methodology, Project administration, Software, Supervision, Validation, Writing – review & editing.

### Acknowledgements

O.S. thanks Azam Karimimamaghan for assistance with the implementation of the binning algorithm for identifying pairs of particles within a specified distance of each other. This research was conducted with the financial support of the Synthesis and Solid State Pharmaceutical Centre (SSPC), funded by the Science Foundation Ireland (SFI) and co-funded by the European Regional Development Fund under Grant Number 14/SP/2750. We thank the Irish Centre for High-End Computing (ICHEC) for the provision of computational facilities and support.

### Appendix A. Lubrication forces and torques between particles and walls

During sub-grid scale collisions, the particles interact not only with the neighbouring particles, but also come into close proximity of the top and bottom walls. Therefore, in this appendix, the modelling equations for both normal and tangential lubrication forces and torques on a particle during its interaction with either wall are provided. By taking

$\alpha \rightarrow \infty$  in Eqs. (1) through (3b) and by replacing  $q$  with  $w$ , the lubrication equations are derived as

$$\frac{\mathbf{F}_p^{w,n}}{6\pi\mu R_{hyd}^2} = \left(\frac{1}{h} - \frac{1}{h_o^n}\right) \mathbf{U}_n, \quad (\text{A.1a})$$

$$\frac{\mathbf{F}_p^{w,t}}{6\pi\mu R_{hyd}} = \left(\frac{8}{15}\right) \ln\left(\frac{h}{h_o^{tw}}\right) \mathbf{U}_t, \quad (\text{A.1b})$$

$$\frac{\mathbf{F}_p^{w,r}}{6\pi\mu R_{hyd}^2} = \left(\frac{2}{15}\right) \ln\left(\frac{h}{h_o^{rw}}\right) (\boldsymbol{\omega}^F \times \hat{\mathbf{n}}_{pw}), \quad (\text{A.1c})$$

and

$$\frac{\mathbf{T}_p^{w,t}}{8\pi\mu R_{hyd}^2} = \left(\frac{1}{10}\right) \ln\left(\frac{h}{h_o^{tw}}\right) (\hat{\mathbf{n}}_{pw} \times \mathbf{U}_{pw}), \quad (\text{A.2a})$$

$$\frac{\mathbf{T}_p^{w,r}}{8\pi\mu R_{hyd}^3} = \left(\frac{2}{5}\right) \ln\left(\frac{h}{h_o^{rw}}\right) \boldsymbol{\omega}^T. \quad (\text{A.2b})$$

In Eqs. (A.1a) through (A.2b), the definition of the translational and rotational velocities remains the same as previously discussed in Section 3.2, except that  $q$  is now replaced with  $w$ . These additional particle–wall lubrication corrections are individually enabled when the gap between any particle and either wall is below  $h_o^n$ ,  $h_o^{tw}$ , and  $h_o^{rw}$ , respectively. Both  $h_o^{tw}$  and  $h_o^{rw}$  were computed by simulating the translation and rotation of a single sphere at several interparticle distances away from the wall, and the above particle–wall force and torque contributions are added as,

$$\mathbf{F}_p^{w,lub} = \mathbf{F}_p^{w,n} + \mathbf{F}_p^{w,t} + \mathbf{F}_p^{w,r}, \quad (\text{A.3a})$$

$$\mathbf{T}_p^{w,lub} = \mathbf{T}_p^{w,t} + \mathbf{T}_p^{w,r} \quad (\text{A.3b})$$

to obtain the overall lubrication contribution as given in Eqs. (4a) and (4b).

### Appendix B. Initialising the particle positions

This appendix discusses several approaches used to initialise the particle positions. For suspensions up to 38% solids, random initialisation of the particle positions was implemented. In this method, random points are selected and those that overlap with the existing particles are rejected. Using this approach, non-overlapping spheres (within the simulation domain as well as across the periodic boundary) up to a limit of 35% solids (i.e.  $N_p = 280$ ) were attainable. In order to achieve solids up to 38% by volume ( $N_p = 310$ ), the same approach was used except that overlaps were accepted across the periodic boundary. Then we used the spring-like repulsive force [1] to separate the overlap.

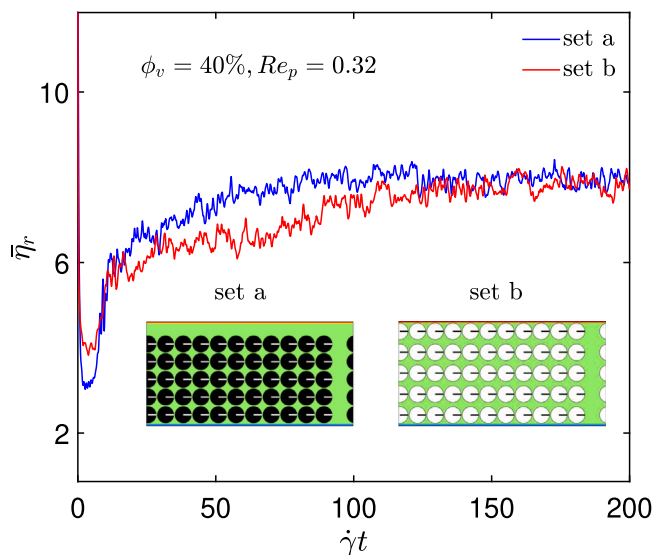


Fig. B.1. Differences in the evolution of the relative apparent viscosity of a suspension as a function of dimensionless time for two different initial particle configurations (set a and set b). For this example,  $\phi_v = 40\%$  and  $Re_p = 0.32$ , and only normal lubrication corrections were included. The insets show the two initial conditions.

For  $\phi_v = 40\%$ , we used a regular cubic packing and considered two different configurations as presented in Fig. B.1. In the first configuration (set a), we stacked the spheres with a gap of 0.4 lu which left additional gaps near  $x = L$ ,  $y = W$ , and  $z = H$  (7 lu, 1.5 lu, and 6.67 lu, respectively). In the second case (set b), we retained the large gap near the periodic boundaries ( $x = L$  and  $y = W$ ) and stretched the gaps along the wall-normal  $z$  direction while maintaining a gap of 0.5 lu between the particles and the top and bottom walls. The inset in Fig. B.1 shows cross-sections through the two initial particle configurations. Both suspensions started from rest and were sheared until steady-state. While the suspensions attain approximately the same viscosity in the long run (the difference is  $\approx 4\%$ ), the evolution of the viscosity towards this equilibrium depends on the initial particle configuration. Finally, to achieve 47% solids by volume, we specified the initial positions of the spheres by using a cubic packing with small random displacements.

For simulations up to 38% solids, the simulation domain was  $100 \times 50 \times 50$  lu. In order to handle more particles at higher concentrations, we slightly altered the domain size by increasing the dimension along the  $x$ ,  $y$ , and  $z$  directions to 100, 52, and 50 lu for 40% solids, and 102, 52, and 54 lu for 47% solids, respectively. A grid independence study has been previously reported [1], and our results are not sensitive to increases in domain size along the periodic boundaries as well as across the channel height. Therefore, a domain size of  $100 \times 50 \times 50$  lu with particles of  $R = 4$  lu is sufficient to represent larger domains.

## References

- [1] Srinivasan S, Van den Akker HEA, Shardt O. Shear thickening and history-dependent rheology of monodisperse suspensions with finite inertia via an immersed boundary lattice Boltzmann method. *Int J Multiph Flow* 2020;125:103205.
- [2] Brady JF, Bossis G. The rheology of concentrated suspensions of spheres in simple shear flow by numerical simulation. *J Fluid Mech* 1985;155:105–29.

- [3] Jogun S, Zukoski CF. Rheology of dense suspensions of plate-like particles. *J Rheol* 1996;40(6):1211–32.
- [4] Stickel JJ, Powell RL. Fluid mechanics and rheology of dense suspensions. *Annu Rev Fluid Mech* 2005;37:129–49.
- [5] Guazzelli E. Rheology of dense suspensions of non colloidal particles. In: EPJ web of conferences. vol. 140, EDP Sciences; 2017, p. 01001.
- [6] Simon DB, Hormozi S, Guazzelli E, Pouliquen O. Rheology of dense suspensions of non-colloidal spheres in yield-stress fluids. *J Fluid Mech* 2015;776.
- [7] Lorenz E, Sivasadan V, Bonn D, Hoekstra AG. Combined lattice-Boltzmann and rigid-body method for simulations of shear-thickening dense suspensions of hard particles. *Comput & Fluids* 2018;172:474–82.
- [8] Thorimbert Y, Marson F, Parmigiani A, Chopard B, Lätt J. Lattice Boltzmann simulation of dense rigid spherical particle suspensions using immersed boundary method. *Comput & Fluids* 2018;166:286–94.
- [9] Bergholtz J, Brady JF, Vicol M. The non-Newtonian rheology of dilute colloidal suspensions. *J Fluid Mech* 2002;456:239–75.
- [10] Kulkarni PM, Morris JF. Suspension properties at finite Reynolds number from simulated shear flow. *Phys Fluids* 2008;20(4):040602.
- [11] Fall A, Lemaître A, Bertrand F, Bonn D, Ovarlez G. Shear thickening and migration in granular suspensions. *Phys Rev Lett* 2010;105(26):268303.
- [12] Dbouk T, Lobry L, Lemaire E. Normal stresses in concentrated non-Brownian suspensions. *J Fluid Mech* 2013;715:239–72.
- [13] Brown E, Jaeger HM. Shear thickening in concentrated suspensions: phenomenology, mechanisms and relations to jamming. *Rep Progr Phys* 2014;77(4):046602.
- [14] Gadala-Maria F, Acrivos A. Shear-induced structure in a concentrated suspension of solid spheres. *J Rheol* 1980;24(6):799–814.
- [15] Kolli VG, Pollauf EJ, Gadala-Maria F. Transient normal stress response in a concentrated suspension of spherical particles. *J Rheol* 2002;46(1):321–34.
- [16] Blanc F, Peters F, Lemaire E. Local transient rheological behavior of concentrated suspensions. *J Rheol* 2011;55(4):835–54.
- [17] Peters F, Ghigliotti G, Gallier S, Blanc F, Lemaire E, Lobry L. Rheology of non-Brownian suspensions of rough frictional particles under shear reversal: A numerical study. *J Rheol* 2016;60(4):715–32.
- [18] O'Neill ME, Majumdar R. Asymmetrical slow viscous fluid motions caused by the translation or rotation of two spheres. Part 1. The determination of exact solutions for any values of the ratio of radii and separation parameters. *Z Angew Math Phys* 1970;21(2):164–79.
- [19] Nguyen NQ, Ladd AJC. Lubrication corrections for lattice-Boltzmann simulations of particle suspensions. *Phys Rev E* 2002;66(4):046708.
- [20] Simeonov JA, Calantoni J. Modeling mechanical contact and lubrication in direct numerical simulations of colliding particles. *Int J Multiph Flow* 2012;46:38–53.
- [21] Krieger IM, Dougherty TJ. A mechanism for non-Newtonian flow in suspensions of rigid spheres. *Trans Soc Rheol* 1959;3(1):137–52.
- [22] Chen S, Doolen GD. Lattice Boltzmann method for fluid flows. *Annu Rev Fluid Mech* 1998;30(1):329–64.
- [23] Feng ZG, Michaelides EE. The immersed boundary-lattice Boltzmann method for solving fluid-particles interaction problems. *J Comput Phys* 2004;195(2):602–28.
- [24] Ladd AJC. Numerical simulations of particulate suspensions via a discretized Boltzmann equation. Part 1. Theoretical foundation. *J Fluid Mech* 1994;271:285–309.
- [25] Ladd AJC. Numerical simulations of particulate suspensions via a discretized Boltzmann equation. Part 2. Numerical results. *J Fluid Mech* 1994;271:311–39.
- [26] Krüger T, Kusumaatmaja H, Kuzmin A, Shardt O, Silva G, Viggen EM. The lattice Boltzmann method: Principles and practice. Springer; 2017.
- [27] Shan X, Chen H. Lattice Boltzmann model for simulating flows with multiple phases and components. *Phys Rev E* 1993;47(3):1815.
- [28] Derksen JJ, Sundaresan S. Direct numerical simulations of dense suspensions: wave instabilities in liquid-fluidized beds. *J Fluid Mech* 2007;587:303–36.
- [29] Krüger T, Varnik F, Raabe D. Efficient and accurate simulations of deformable particles immersed in a fluid using a combined immersed boundary lattice Boltzmann finite element method. *Comput Math Appl* 2011;61(12):3485–505.
- [30] Ten Cate A, Derksen JJ, Portela LM, Van den Akker HEA. Fully resolved simulations of colliding monodisperse spheres in forced isotropic turbulence. *J Fluid Mech* 2004;519:233–71.
- [31] Bird RB, Stewart WE, Lightfoot EN. Transport phenomena. John Wiley & Sons; 2007.
- [32] Sierou A, Brady JF. Rheology and microstructure in concentrated noncolloidal suspensions. *J Rheol* 2002;46(5):1031–56.